Declaration

I hereby declare that the work presented in this Thesis titled ***Modified 2D MoS_2 and SnS_2 Flakes for Sensing Applications*** submitted to the Indian Institute of Technology Jodhpur in partial fulfilment of the requirements for the award of the degree of Doctor of Philosophy, is a bonafide record of the research work carried out under the supervision of Professor Mahesh Kumar. The contents of this thesis in full or in parts, have not been submitted to, and will not be submitted by me to, any other Institute or University in India or abroad for the award of any degree or diploma.



Ashok Kumar
P19EE203

Certificate

This is to certify that the thesis titled ***Modified 2D MoS_2 and SnS_2 Flakes for Sensing Applications***, submitted by *Ashok Kumar* (P19EE203) to the Indian Institute of Technology Jodhpur for the award of the degree of *Doctor of Philosophy*, is a bonafide record of the research work done by him under my supervision. To the best of my knowledge, the contents of this report, in full or in parts, have not been submitted to any other Institute or University for the award of any degree or diploma.

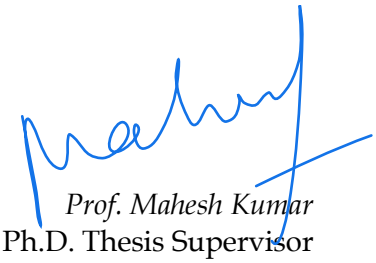

Prof. Mahesh Kumar
Ph.D. Thesis Supervisor
Department of Electrical Engineering
IIT Jodhpur, India

Acknowledgements

First, I would like to express my sincere gratitude to my supervisor, *Professor Mahesh Kumar*, for his consistent guidance and motivation. He has been a constant support of encouragement, and his exceptional research aptitude plays a crucial role in the success of this thesis work. Without his support, this work would not have been possible. He is always open to discussion and tried his best to provide a good research environment and facilities to work in the lab. I acquired valuable insights from him about investigating and interpreting experimental data, and his confidence in my work inspired me to strive for better outcomes. He always pushes to think high and achieve goals in life. It was an incredibly fortunate and unforgettable experience to have the opportunity to work under his reflective and revered guidance. His optimistic nature and boundless kindness cannot be fully expressed in words, but I am immensely grateful for his unwavering support throughout this journey.

Also, I am thankful to the members of the Doctoral Committee, *Professor Shree Prakash Tiwari, Professor Manikandan Paranjothy* and *Professor Satyajit Sahu*, for their guidance and support during this research work. I am also thankful to all faculty and staff members of the Department of Electrical Engineering for their constant support during my tenure.

I sincerely acknowledge our collaborators, *Professor Pradeep Kumar* (IIT Mandi, India), *Professor Mukesh Kumar* (IIT Ropar, India), and *Professor Michael S. Strano* from Department of Chemical Engineering, Massachusetts Institute of Technology, Cambridge, Massachusetts, United States for sharing their labs facilities and their contribution in carrying out present thesis work.

My funding agencies, the Prime Minister Research Fellowship, MHRD fellowship, and SERB-International Travel Grant for financially supporting my research work. I am highly grateful to the Centre for Research & Development of Scientific Instruments (CRDSI at IIT Jodhpur for providing characterization facilities. Additionally, I appreciate the support provided by the technical staff/ operators, Mr. Pawan Sharma (FE-SEM and XRD), Mr. Mukesh Rajpurohit (SEM, UV-Vis Spectrometer), and Mr. Sanjay Nimbark (Raman). I gratefully acknowledge Mr. Ummed Singh Rathore, Sr. Assistant, Department of Electrical Engineering, for smoothly carrying up all the documentation work. Also, I would like to thank the Library, IIT Jodhpur, for granting me access to research papers and books essential to my work.

Additionally, my heartfelt gratitude goes out to my colleagues and alumni of the Nanosensors Research Group lab. I am highly grateful to the Doctoral group (Dr. Rahul Kumar, Dr. Neeraj Goel, Dr. Vijendra Bhati, Dr. Sapna Ranwa, Dr. Adarsh Nigam, Dr. Amit Shringi, Dr. Nipun Sharma and Dr. Surajit Das) for their discussions and suggestions. I want to thank my laboratory mates and juniors: Amit, Sumit, Ruksana, Vikas, Jai Mishra, Suraj Barala, Mubashir, Suresh, Arpita, Chayan, Pooja, Kishan, Rovins for their assistance in the lab activities. It was wonderful to work with you all and I really appreciate the time, when we worked together in the lab. Everyone owes a special place in my heart that I cannot express in a few words. I have learned a lot from you all. Apart from that, I really cherished those parties that we were having outside the lab. I want to thank Dr. Chandra Prakash, Dr. Ramavtar, Dr. Kiran, Dr. Mohammad Rahil, Anil Lodhi, Shalu Saini, Anurag, Gargi, Saqib, Somnath, Vandana, Ankit, Dibyajyoti, Minakshi, Priyanka for his assistance in many lab activities. I am grateful to Miss. Neelu Sharma and Mr. Akash Popat Gutkal Ghosh for their contribution to my research article.

Also, I am highly thankful to Prof. Sandeep Yadav, Prof. Ankur Gupta, Prof. Chandan Pandey, Ganapat Choudhary, Kamal Kishore and Shubham Pandey for always being supportive

and keeping me motivated. They are more like a friend or brother to me, and I really enjoyed her company during campus life.

First and foremost, I would like to express my deepest gratitude to my parents, whose unwavering support, unconditional love, and sacrifices have been the foundation of all my achievements. Their guidance and encouragement throughout my journey have been my constant source of strength and inspiration. To my beloved wife Ms. Leela, your patience, understanding, and belief in me during the most challenging times have been immeasurable. Your love and unwavering support have provided me with the motivation and focus to persevere through this journey. I am deeply grateful for all the sacrifices you made to help me succeed. To my dear son Master Ishan Patel, you are my pride and joy. Your smiles and laughter have been a source of relief and happiness during stressful times. You remind me of the importance of balance and joy in life. I would also like to extend my heartfelt gratitude to my uncle, Day Ram Patel, for his unconditional support, encouragement, and guidance. Your blessings and belief in me have been a source of strength throughout this journey. I am also profoundly thankful to my brother, Mr. Rajendra Pal, and Dr. Ram Nivas for his constant encouragement and unwavering belief in me. Your words of motivation have always pushed me to give my best.

At last, I am thankful to the almighty God for his blessings and making me capable of completing this task successfully.

Ashok Kumar
Ph.D. Student

Abstract

The emergence of two-dimensional (2D) transition metal dichalcogenides (TMDCs), particularly SnS_2 and MoS_2, has sparked significant interest in the field of advanced materials due to their unique layered architecture and atomic-scale thickness. These materials exhibit exceptional electrical, optical, and chemical properties, rendering them highly suitable for a wide range of applications, including sensors, photodetectors, and various optoelectronic devices. However, the full potential of SnS_2 and MoS_2 is often hindered by common challenges such as large-area controlled growth, limited optical absorption in pristine materials, and slow response and recovery times attributed to inefficient charge transfer dynamics.

To address these challenges, we employed a thermal chemical vapor deposition (CVD) technique to optimize the growth conditions for high-quality SnS_2 and MoS_2 films. By systematically adjusting parameters, we achieved vertically aligned structures and uniform layers, laying the groundwork for enhanced device performance. Comprehensive characterization techniques, including scanning electron microscopy (SEM), X-ray diffraction (XRD), energy dispersive X-ray spectroscopy (EDX), X-ray photoelectron spectroscopy (XPS), Raman spectroscopy, and photoluminescence (PL) were utilized to analyze and confirm the structural, morphological, and optical properties of the synthesized materials. Based on the results from these analyses, we propose a detailed growth mechanism in which in-plane SnS_2 and mixed MoS_2 flakes acts as a seed layer for the initial development of vertically aligned SnS_2 and MoS_2, ultimately leading to the formation of an interconnected three-dimensional network of these flakes.

We developed a highly sensitive gas sensor based on vertically aligned SnS_2 flakes, which exhibited exceptional selectivity toward NO_2 over various other toxic and combustible gases[Kumar et al., 2022]. The sensor demonstrated stable performance and strong selectivity, supported by electronic structure calculations. To further enhance gas sensing capabilities, we implemented defect and interface engineering techniques, specifically inducing optimal sulfur vacancies in the SnS_2 lattice through nitrogen plasma treatment[Kumar et al., 2023a]. This vacancy engineering significantly improved electronic conductivity and increased the active surface area for gas adsorption, resulting in a remarkable sensitivity to NO_2 and complete recovery at 120°C.

In parallel, we explored the functionalization of mixed MoS_2 flakes for NO_2 gas sensing. Recognizing the limitations of pristine MoS_2, which suffers from low response and slow recovery times, we modified the material through nitrogen doping and decoration with silver nanoparticles. The resulting nitrogen-doped MoS_2 (N-MoS_2) and silver-decorated nitrogen-doped MoS_2 (Ag-N-MoS_2) sensors exhibited substantial improvements in NO_2 sensing performance. Notably, the Ag-N-MoS_2 sensor demonstrated nearly double the response of pristine MoS_2 at 100°C, illustrating the synergistic effects of nitrogen doping and silver decoration.

Finally, we investigated the application of MoS_2 in optoelectronic systems through the development of a self-powered broadband photodetector utilizing a van der Waals heterostructure composed of MoS_2 and WS_2. The fabricated heterostructures exhibited enhanced responsivity, detectivity, and response times compared to pristine MoS_2, showcasing the potential of these materials in next-generation optoelectronic applications. Furthermore, the anticipated challenges and future perspectives in the rapidly evolving research on SnS_2 and MoS_2 for sensing applications are similarly explored.

Contents

		page
Acknowledgements		v
Abstract		vii
Contents		ix-xi
List of Figures		xii-xvii
List of Tables		xviii
List of Symbols		xix
List of Abbreviations		xx-xxi

Chapter 1: Introduction

1.1	Background	1
1.2	Molybdenum disulfide (MoS_2) and Tin disulfide (SnS_2)	3
	1.2.1 Properties of MoS_2	3
	1.2.2 Properties of SnS_2	10
1.3	Synthesis of 2D materials	13
	1.3.1 Top-Down Approach	14
	1.3.2 Bottom-up Approach	16
1.4	Gas Sensor	18
	1.4.1 NO2 Gas Sensor	19
	1.4.2 Classification of gas sensors	20
	1.4.3 Characteristics of Gas Sensor	21
1.5	Gas Sensing Mechanism of 2D Materials	22
1.6	Literature Review on MoS_2 and SnS_2 Gas Sensor	24
1.7	Photodetector	28
	1.7.1 The Figure of Merits of a Photodetector	28
	1.7.2 Photodetector Mechanism	30
1.8	Literature survey on photodetectors based on MoS_2	32
1.9	Challenges and Motivation	34
1.10	Objective of the present thesis work	36
1.11	Outline of Thesis	36

Chapter 2: Fabrication and Characterization of Materials and Devices

2.1	Deposition techniques	39
	2.1.1 Chemical Vapor Deposition (CVD)	39
	2.1.2 Magnetron sputtering	41
	2.1.2 Thermal Evaporation	42
2.2	Characterization Techniques	44
	2.2.1 Field Emission Scanning Electron Microscopy (FESEM)	44
	2.2.2 Energy Dispersive X-Ray Analysis Spectroscopy (EDX)	45
	2.2.3 Raman Spectroscopy	45
	2.2.4 X-ray Photoelectron Spectroscopy (XPS)	46
	2.2.5 Photoluminescence Spectroscopy (PL)	47
	2.2.6 Ultraviolet-Visible (UV-VIS) Spectroscopy	48

2.2.7 X-ray Diffraction (XRD) 49
2.2.8 Kelvin probe force microscopy (KPFM) 50
2.3 Plasma treatment 51
2.4 Device fabrication and characterization 52
2.4.1 Deposition of Metal Contact Using Thermal Evaporation 52
2.4.2 Gas Sensing Measurement 53
2.4.3 Photodetector measurement 53

Chapter 3: Growth and Characterization of MoS_2 and Sns_2 Flakes
3.1 Necessity and Challenges for Controlled growth of MoS_2 and SnS_2 Flakes 55
3.2 *Growth of MoS_2 and SnS_2 Flakes by CVD Method* 56
3.2.1 Synthesis of MoS_2 Flakes 56
3.2.2 Characterizations of MoS_2 Flakes 57
3.2.3 Synthesis of vertically Aligned SnS_2 flakes 59
3.2.4 Characterizations of SnS_2 Flakes 60
3.3 Proposed Growth Mechanism 62
3.4 Synthesis of WS_2 64
3.5 Nitrogen Plasma Treatment 65
3.6 Synthesis of Silver Nanoparticles Using DC Sputtering Technique 66
3.7 Device Fabrication Process 67
3.5 Summary 68

Chapter 4: Effects on Gas Sensing Characteristics of MoS_2 flakes using Surface and Structural Modifications
4.1 Requirement of Fast highly response NO_2 Gas Sensor and Challenges 69
4.2 Synthesis and Fabrication of Ag NPs anchored-nitrogen plasma treated MoS_2 flakes 71
4.3 Results and Discussion 71
4.3.1 Structure and chemical properties 71
4.3.2 NO_2 Gas Sensing Performance of MoS2 Flakes 74
4.3.3 Effect of nitrogen plasma treatment on MoS2 (N-MoS_2) Flakes toward NO_2 Gas Sensing Performance 76
4.3.4 Effect of surface functionalization of silver nanoparticles (Ag NPs) on pristine-MoS_2 and N-MoS2 Flakes toward NO_2 Gas Sensing Performance 77
4.3.5 Response and recovery time of the pristine-MoS_2, Ag-MoS_2, N-MoS_2 and Ag-N-MoS_2 sensors 78
4.4 Long-term stability, Effect of Humidity, Short-term repeatability, and Selectivity of MoS_2 sensors 79
4.5 Gas sensing mechanism 81
4.5 Summary 82

Chapter 5: Improved Gas Sensing Performance of SnS_2 via Defect Engineering
5.1 Requirement of highly selective and high response NO_2 Gas Sensor and Challenges 83
5.2 Synthesis, and nitrogen plasma treatment of Vertically Aligned SnS_2 flakes 85
5.3 Characterization 85
5.3.1 Structure and chemical properties of SnS_2 flakes 85
5.3.2 Vacancy and Doping Investigation using FE-SEM Raman Spectroscopy, and XPS 86
5.4 Gas Sensing Properties of Vertically Aligned SnS_2 Flakes 88
5.4.1 Optimization of the operating temperature and Static response behaviour VA-SnS_2 88
5.4.2 Repeatability, Response time, Selectivity, and Limit of Detection of VA-SnS_2 sensor 90

5.4.3 Effect of humidity 91
5.4.4 Gas sensing mechanism 93
5.5 Effects of Vacancy on Gas Sensing Characteristics of Vertically Aligned SnS_2 Flake 94
5.5.1 I-V characteristics and surface resistances 94
5.5.2 Static response behaviour Vs-SnS_2 sensor 95
5.5.3 Repeatability, Selectivity, Response time, and Limit of Detection of Vs-SnS_2 sensor 96
5.5.4 Gas sensing mechanism 98
5.6 Summary 100

Chapter 6: DFT studies and Gas Sensor Modelling
6.1 Requirement of Theoretical Investigations of NO_2 Adsorption 101
6.2 Vienna Ab initio Simulation Package (VASP) 102
6.3 Computational Method 103
6.3.1 Ag NPs anchored-nitrogen plasma treated MoS_2 (Ag-N-MoS_2) flakes 103
6.3.2 Vertically Aligned SnS_2 (VA-Sn_{S2}) flakes 103
6.3.3 Vacancy-Assisted Vertically Aligned SnS_2 (Vs-SnS_2) flakes 103
6.4 Result and Discussion 104
6.4.1 Adsorption properties of Ag NPs anchored-nitrogen plasma treated Mo_{S2} (Ag-N-MoS_2) flakes 104
6.4.2 Adsorption properties of Vertically Aligned SnS_2 (VA-SnS_2) flakes 106
6.4.3 Adsorption properties of Vacancy-Assisted Vertically Aligned SnS_2 (Vs-SnS_2) flakes 107
6.5 Gas sensor modelling 109
6.5.1 Gas adsorption-desorption kinetics in 2D material 109
6.5.2 Transient response cycles with fitting curve of Pristine SnS_2 flakes 111
6.5.3 Transient response curve with fitting curve of nitrogen plasma treated SnS_2 flakes 111
6.6 Summary 114

Chapter 7: High-Performance Broadband Photodetector Based on MoS_2-WS_2 Heterojunction
7.1 Requirement of highly sensitive, fast, and broadband photodetectors 115
7.2 Device fabrication from MoS2-WS2 heterojunction and light-sensing experimental details 116
7.3 Characterization of MoS_2-WS_2 heterojunctions 117
7.4 Effects of visible to near-infrared wavelength on the MoS_2-WS_2 heterojunctions 119
7.5 Speed and stability of the photodetector 123
7.6 Self-powered functionality of CVD-synthesized MoS_2 photodetector 124
7.7 Light sensing mechanism of the photodetector 127
7.8 Summary 128

Chapter 8: Conclusions and Future Scope
8.1 Conclusions 129
8.2 Scope for Future Work 131

List of Publication 133
References 135

List of Figures

Figures	*Title*	*page*
1.1	(a) Transition metal dichalcogenides materials in the periodic table that form layered materials and an example of 2D materials, (b) Stacking of hexagonally packed planes bounded by the van der Waals force. Possible coordination unit of layered TMDs, and (c) Trigonal prismatic (AbA) (d) Octahedron (AbC)	*3*
1.2	Crystal structures of MoS2 polymorphs. (a) 1T phase (octahedral), (b) 2H phase (trigonal prismatic) and (c) 3R phase (trigonal prismatic).	*4*
1.3	Crystal structure of MoS_2 (a) 2H phase (b) 1T phase, with a schematic representation of the gradual filling of d orbitals that are situated in the bandgap between bonding (σ) and anti-bonding states (σ*)	*5*
1.4	(a) Top view of the 2H-MoS_2 structure. (b) Corresponding Brillouin zones for the 2H-MoS_2. Theoretically calculated band structures for the (c) Bulk MoS_2 and quadrilateral MoS2. (d) Schematics of orbitals combinations of CBM and VBM electronic states and corresponding Mo and S orbitals for bulk MoS_2. Band structures for the (e) Bilayer MoS_2 and monolayer MoS2. (f) Schematics of orbitals combinations of CBM and VBM electronic states and corresponding Mo and S orbitals for monolayer MoS_2.	*6*
1.5	(a) Two Raman (A_{1g} and $E_{2g}{}^1$) active mode in mono and few-layers MoS_2, and (b) All possible vibrational modes ($E_{2g}{}^2$, E_{1g}, $E_{2g}{}^1$, A_{1g} and $E_{1u}{}^1$, $A_{2u}{}^1$) in bulk MoS_2.	*7*
1.6	(a) Optical absorption spectra for MoS_2 from monolayer to six layers, and (b) The absorption coefficient was calculated for the MoS_2.	*8*
1.7	(a) Band structure of the bulk and monolayer MoS_2, where A and B indicate the direct-gap transitions, and I represent the indirect-gap transition. The indirect gap for the bulk is denoted by $E_g{}'$ and direct gap for the monolayer is indicated as E_g. (b) Schematic for excitons and trions. (c) PL spectra for mono and bilayer MoS_2, inset displaying the relative quantum yield of MoS_2 as a function of layer number, (d) The normalized PL spectra with respect to layer number. (e) Schematic illustration of the optical transition occurring at the K-point of the Brillouin zone in different regions of MoS_2, including monolayer, bilayer, and bulk. The A exciton peak experiences a red shift due to the reduction of the first exciton level. The B-exciton peak position remains relatively the same because the decrease in the exciton level is balanced by an increase in the valence band splitting energy.	*9*
1.8	Properties of SnS_2. (a) Crystal structure, (b) band position, and (c) Band position of SnS_2 for photocatalytic reactions.	*11*
1.9	Side view and top view of ball and stick model schematic diagram of SnS_2	*12*
1.10	((a, b) Optical absorption spectra temperature corresponding to direct and indirect energy band gaps for a crystal structure of SnS_2. (c) Raman spectra of SnS_2 at varying temperature (150 °C for 1 h, 150 °C for 2 h, and 300 °C for 1 h).	*13*
1.11	Schematic image of top-down approach for synthesis of 2D material (a) mechanically exfoliated MoS_2 (Scotch tape method), (b) Electrochemical lithiation process, (c) Liquid exfoliation method, and (d) Sputtering.	*15*
1.12	Schematic illustration of different bottom-up methods for the synthesis and growth of 2D material	*17*
1.13	Schematic representation of a gas sensor	*19*
1.14	Classification of the gas sensor based on sensing operation principles.	*20*
1.15	Schematics of gas sensing mechanism of in 2D material-based gas sensors.	*24*
1.16	Schematic of a photodetector device	*28*

1.17	Schematic diagram of photoconductive effect (a) without illumination and under external bias, (b) under illumination with energy of photons (Eph), (c) IDS – Vg curves under light (solid red line) and in the dark (solid blue line), (d) traces of IDS – VDS in the dark (solid blue line) and when illuminated (solid red line), (e) Schematic view of photogating effect.	30
1.18	(a), (b) Schematic view of photovoltaic effect arising from a metal–semiconductor Schottky barrier and p–n junction, and (c) IDS – VDS traces in the dark (solid black line) and under illumination (solid red line).	31
2.1	(a) Schematic illustration of the CVD steps, and (b) Optical images of thermal chemical vapor deposition (CVD) system which is used for this thesis work	41
2.2	(a) Schematic representation of the RF sputtering system, and (b) Optical images of sputtering system at the microfabrication lab, IIT Jodhpur.	42
2.3	(a) Schematic illustration of the thermal evaporation system, and (b) Optical images of Thermal evaporation system at Microfabrication lab, IIT Jodhpur	43
2.4	(a) Schematic representation of working of FESEM, and (b) Optical images of SEM and FESEM in central facility IIT Jodhpur	44
2.5	(a) Schematic of the XPS setup, which provides both elemental and chemical detail, and (b) Optical images of XPS system, IIT Mandi.	45
2.6	(a) Schematic of the XPS setup, which provides both elemental and chemical detail, and (b) Optical images of XPS system, IIT Mandi.	47
2.7	Schematic of a PL spectroscopy.	47
2.8	(a)Schematic representation of a UV-VIS spectrometer, and (b) Optical images of UV-VIS spectrometer, IIT Jodhpur	48
2.9	(a) Schematic for the X-ray diffraction used to study the crystal structure of the film, (b) Diagram of Bragg's law for X-ray diffraction, and (c) Optical images of X-ray diffraction system (D8 Advance, Bruker) at IIT Jodhpur.	49
2.10	(a) Schematic view of band alignment between the sample and the tip in a typical KPFM set-up under different conditions: Non-contact, External electrical contact, Applied DC voltage, and (b) Optical images of KPFM system at IIT Mandi.	50
2.11	(a) Optical images of RF Plasma chamber	51
2.12	Interdigitated electrode physical shadow mask used for electrode deposition	52
2.13	(a) Schematic illustration of gas sensing setup, and (b) Optical Image of the gas sensing system, which is used for this thesis work.	53
2.14	(a) Schematic representation of the experimental setup used to measure spectral response of MoS2 based photodetectors, and (b) Optical Image of the photodetector system, which is used for this thesis work.	54
3.1	(a) Schematic of thermal chemical vapor deposition (CVD) technique used to grow MoS_2 flakes. SiO_2/Si substrate was placed on top of MoO_3 powder in zone 1, (b) temperature profile for MoO_3 and S powders in Zone 1, Zone 2, respectively and (c, d) Show the different growth conditions and nomenclatures of synthesized sample	57
3.2	SEM images of MoS_2 flakes grow at different deposition temperature (a) 750 °C, (b) 800 °C, (c) 850 °C, and (d) 9000 °C. The flow of argon of 80 sccm keep constant during the growth.	58
3.3	SEM images of MoS_2 flakes grow at different gas flow rates (a) 60 sccm, (b) 70 sccm, (c) 80 sccm and (d) 100 sccm. The growth temperature for all these samples was fixed at 850°C	58
3.4	(a) High-resolution FE-SEM images of CVD grown MoS_2 on SiO2/Si substrate, (b) XRD spectra of optimized MoS_2 flakes, the peaks become sharper, highly intense and with more planes of MoS2, and (c) Raman spectra of the optimized MoS2 flakes. Raman spectra consist of two strong peaks that corresponds to in-plane, E^1_{2g}, and out-of-plane, A_{1g}, vibrations of S- Mo-S atoms	59

3.5	(a) Schematic of the thermal chemical vapour deposition (CVD) technique used in growing SnS_2 flakes. SiO_2/Si substrate place in in zone 3. (b)The temperature profiles of S and SnO_2 powders in zones 1 and 2, respectively and (c, d) illustrate the various growth circumstances (Temperature, gas flow) and grown sample names	60
3.6	SEM images of SnS_2 flakes grow at different deposition temperature (a) 750 °C, (b) 800 °C, (c) 850 °C, and (d) 9000 °C. The flow of argon gas (80 sccm) keep constant during the growth.	61
3.7	SEM images of SnS_2 flakes grow at different gas flow rates (a) 60 sccm, (b) 80 sccm, (c) 100 sccm and (d) 120 sccm. The growth temperature for all these samples was fixed at 1000°C	61
3.8	(a) High-resolution SEM images of CVD grown vertically aligned SnS_2 flakes on SiO_2/Si substrate, (b) Raman spectra of the optimized SnS_2 flakes. Raman spectra consist of two strong peaks that corresponds to in-plane, Eg, and out-of-plane, A1g, vibrations of S- Sn-S atoms, (c) XRD spectra of optimized SnS_2 flakes, the peaks become sharper, highly intense and with more planes of SnS_2.	62
3.9	The suggested growth mechanism for edge-enriched MoS_2 and SnS_2 flakes. (a) Represents the diffusion and absorption stage of in-plane MoS_2 and SnS_2 formation. In this phase, in-plane MoS2 and SnS2 development is more rapid, resulting in the production of monolayer to multilayer flakes on the substrate, (b) Growth of edge-enriched flakes at the nucleation and chemical reaction stage. The incoming S and Mo, Sn atoms adsorb on the substrate and MoS_2 and SnS_2 flakes, causing edge-enriched flakes to develop, (c) Schematic illustration the growth stage for finally as grown interconnected MoS_2 and SnS_2 flakes, and (d) SEM image of the MoS_2 and SnS_2 flakes.	63
3.10	(a) Schematic illustration of WS_2 nanoparticle synthesis using the hydrothermal method, (b) FE-SEM image showing the morphology of the synthesized WS_2 nanoparticles, and (c) Raman spectra confirming the characteristic vibrational modes of WS_2	65
3.11	Schematic illustration of (a) nitrogen plasma treatment and subsequent functionalization with silver (Ag) nanoparticles on CVD-grown MoS_2 flakes, and (b) nitrogen plasma treatment on CVD-grown SnS_2 flakes, showcasing the process of sulfur vacancy creation, nitrogen doping, and nanoparticle deposition to enhance material properties.	66
3.12	Device Fabrication Process for Interdigitated Electrode (IDE) Structures on CVD-grown SnS_2 and MoS_2.	68
4.1	FE-SEM images of (a) Grown MoS2 flakes, (b) High-resolution image of MoS2 flakes, (c) Nitrogen plasma treated MoS2 (N-MoS2) flakes, (d) High magnification view of N-MoS2, (e) Ag NPs anchored N-MoS2 (Ag-N-MoS2) flakes, and (f) High-resolution image of Ag-N-MoS2 flakes. The average size of Ag NPs is 50nm.	72
4.2	Energy dispersive spectroscopy (EDX) elemental mapping of Ag-N-MoS2 sample (a) Area selected, Elemental mapping of (b) Molybdenum (Mo), (c) sulfur (S), (d) Nitrogen (N), and (e) Silver (Ag).	72
4.3	Raman spectra of the pristine MoS2, Ag-MoS2, N-MoS2 and Ag-N-MoS2. (a) High-resolution XPS spectra for the N pristine MoS2, Ag-MoS2, N-MoS2 and Ag-N-MoS2, (b) Mo 3d, (c) S 2p, (d) N1s, and (e) Ag 3d	74
4.4	Optical emission spectra (OES) of atmospheric air SDBD plasma source operated at 5.0 kV/25 kHz, and (b) electron temperature profile at different applied voltage and at a fixed frequency of 25 kHz	75
4.5	(a) Schematic of the Ag NPs-decorated N-MoS2 sensor, (b) Comparison of variation in baseline resistance (absence of gas) and relative response of the pristine-MoS_2 sensor with temperature, (c) Resistance versus time plot of the pristine-MoS2 under exposure to NO2 gas ranging from 50 to 1 ppm at RT, (d) Relative response characteristics of the pristine-MoS2 sensor at RT, (e) Resistance versus time plot of the pristine-MoS2 under exposure to NO2 gas ranging from 50 to 1 ppm at 100 °C, (f) Relative response characteristics of the pristine-MoS2 sensor at 100 °C.	76
4.6	(a) Comparison of response of N0, N1, N5, and N8 sensors for 50 ppm of NO2, respectively, (b) Comparison of baseline resistance and response of N0, N1, N5, and N8 sensors for 50	76

ppm of NO_2, respectively, (c) Real time change in resistance, and (d) Transient relative response of N-MoS_2 device for different concentration of NO_2 at 100 °C

4.7 (a) Comparison of the relative response for pristine MoS_2, nitrogen plasma treated MoS_2 (N-MoS_2), Ag functionalized sensor (Ag-MoS_2, and Ag-N-MoS_2) for 50 ppm of NO_2, (b) Baseline resistance and relative response curve of the pristine MoS_2, Ag-MoS_2, N-MoS_2, and Ag-N-MoS_2 sensors for 50 ppm of NO_2, and (c) Relative response versus different concentration of NO_2 gas curve of the pristine MoS_2, Ag-MoS_2, N-MoS_2, and Ag-N-MoS_2 sensors for 50 ppm of NO_2 at 100 °C, respectively *77*

4.8 Transient relative resistance and response for different concentration of NO_2 at 100 °C (a, b) Ag-MoS_2, and (c, d) Ag-N-MoS_2 *78*

4.9 Response time and Recovery time of sensor under a 50 ppm NO_2 concentration at 100 °C. (a) pristine MoS_2, (b) Ag-MoS_2, (c) N-MoS_2, and (d) Ag-N-MoS_2. *79*

4.10 (a) The long-term stability of the pristine MoS_2, Ag-MoS_2, N-MoS_2, and Ag-N-MoS_2 devices to 50 ppm NO_2 gas at 100 °C, (b) Baseline resistance versus different relative humidity (RH %) of pristine MoS_2, Ag-MoS_2, N-MoS_2, and Ag-N-MoS_2 devices to NO_2 gas at 100 °C, (c) Repeatability of Ag-N-MoS_2 toward 50 ppm of NO_2 gas at 100 °C, and (d) Selectivity performance of pristine MoS_2, Ag-MoS_2, N-MoS_2, and Ag-N-MoS_2 devices to 50 ppm of various gases at 100 °C *80*

4.11 Schematic diagram proposed sensing mechanism. *82*

5.1 (a) SEM images of the vertically aligned SnS_2, (b) a magnified view of the flakes network, (c) Raman spectra of the vertically aligned SnS_2 flakes at 532 nm laser, and (d) X-Ray diffraction pattern of vertically aligned SnS_2 flakes. *85*

5.2 (a) FE-SEM image of the nitrogen plasma treated SnS_2 (Vs-SnS_2) flakes, Energy dispersive spectroscopy (EDX) elemental mapping of Vs-SnS_2 sample (b) Area selected, Elemental mapping of (c) Tin (Sn), (d) sulfur (S), (e) EDX spectrum of Vs-SnS_2 sample. *86*

5.3 (a) Raman spectra of the SnS_2 nanoflakes, and (b) Change in Raman shift and Line width, before and after N_2 plasma treatment of N0, N4, N8, N12 and N16 samples *87*

5.4 XPS spectra from pristine VA- SnS_2 and N_2 plasma treated VA- SnS_2, (a) Sn 3d5/2, (b) Sn 3d3/2, (c) S 2p, and (d) N1s *87*

5.5 (a) Schematic diagram of the fabricated device, (b, c) Real-time change in resistance of the sensor with the temperature at RT, and 120 °C, respectively (d) Response time plot at RT with various concentration of NO_2, (e) Response verses concentration of NO_2 plot at 120 °C, and (f) Response of SnS_2 as a function of NO_2 concentration under room temperature, and 120 °C *89*

5.6 (a) Response at 120 °C with same concentration of 50 ppm of NO_2, (b) Response time plot of single cycle to calculate response time at 120 °C and 50 ppm of NO_2, (c) Response of 50 ppm of NO_2 at various temperature from RT to 120 °C, (d) Selectivity test histogram of NO_2, H_2S, H_2, NH_3, CO, CO_2, and CH_4 gas, (e) Response and recovery time as a function of NO_2 concentration (5-5- ppm) at 120 °C, and (f) Limit of detection calculation for NO_2 gas *90*

5.7 (a) Variation of baseline resistance with relative humidity from 25% to 75% for vertically aligned SnS_2 flakes at 120 °C, and (b) Response variations when SnS_2 gas sensor exposed to 50 ppm NO_2 under different relative humidity conditions at 120 °C. *93*

5.8 Schematic representation of sensing mechanism of the SnS_2 flakes *94*

5.9 (a) Schematic illustration and SEM image of the fabricated Vs-SnS_2 device, (b) Linear I-V plots of the pristine SnS_2 sensor at RT and 120 °C, respectively, (c) I-V plots of the pristine SnS_2 and plasma treated SnS_2 (N4, N8, N12 and N16) samples sensor at 120 °C, respectively, and (d) Variation of baseline resistance at different interval of N_2 plasma (N0, N4, N8, N12, and N16) at 120 °C. *95*

5.10 (a) Comparison of response of N0, N4, N8, N12, and N16 sensors for 50 ppm of NO_2 concentrations, respectively, (b) Comparison of the gas responses of N0, N4, N8, N12 and N16 samples at temperature 120 oC for 50 ppm NO_2 gas, (c) Sensing response of N12 device toward NO_2 gas at concentrations ranging from 1 to 50 ppm under the operation *96*

temperature of 120 °C, and (d) Response–concentration plot of pristine SnS_2 and Vs-SnS_2 (N12)samples

5.11 (a) Vs-SnS_2 sensor repeatability for 50 ppm gas at 120 °C, (b) Selectivity of sensor to 50 ppm different gases at 120 °C, (c) Response time and Recovery time of N12 gas sensor under a 50 ppm NO_2 concentration at 120 °C, and (d) Response versus NO_2 concentration curve. (Inset) Linear fitting curve of N12 sample of SnS_2 (12 min plasma treatment) at 120 oC, for calculation of the Limit of detection (LoD). *97*

5.12 Schematic illustration of the sensing mechanism for the boosted gas response to NO_2 *99*

6.1 The top and side views of NO_2 gas adsorption on the (a) pristine MoS_2 (b) N-MoS_2 and (c) Ag decorated N-MoS_2, and (d) Histogram of adsorption energy pristine MoS_2, N-MoS_2, Ag decorated N-MoS_2, for NO_2 gas. *104*

6.2 (a) The top and side view of a unit cell of monolayer SnS_2, (b) Optimized N atom of NO_2 molecule is adsorbed onto the surfaces of SnS_2 top and side view, (c) Other gases CO_2, H_2S and H_2 kept similar fashion giving optimised structures (1)- (3), and (d) Histogram of adsorption energy for NO_2, CO_2, H_2S and H_2 gas *106*

6.3 Computational model geometries of gas surface system. (a) Initial and optimized structures (from top and side view) of gas-monolayer adsorption system with NO_2 above the sulfur vacant sites with supercell containing single vacant site (I), (b) conjugated double vacant sites (II), and (c) Nitrogen doped single vacant site (III) *108*

6.4 (a) Histogram of adsorption energy for pristine (SnS_2), structure containing sulfur vacant site (Vs-SnS_2) and Nitrogen doped monolayer with sulfur vacant site(N2-Vs-SnS_2), (b) Histogram of adsorption energy for NO_2, CO_2, and H_2S gas, and optimized structures of other gases (c) CO_2, and (d) H_2S. *109*

6.5 Irreversible Adsorption: Experimental (scattered point) and fitted (solid dashed red line) response of VA-SnS_2 based sensor to NO_2 gases for different concentration (5-50ppm) at (a-c) RT, and 120 °C. *111*

6.6 Irreversible Adsorption (Nonlinear fit model): Response transients of nitrogen plasma treated SnS_2 (Vs-SnS_2) samples are plotted as a function of (Cat) vs log response the points collapse to a single model operating at 120 oC (a, b) N4 sample, (c, d) N8 sample, (e, f, g) N12 sample, and (h, i) N16 sample, fitted (red color short dashed line), respectively *112*

7.1 (a) FE-SEM image of WS_2 nanoparticles decorated MoS_2 flakes network, (b, c, d) EDX element mapping pictures of the MoS_2-WS_2, confirming the existence of Mo, W and S. *117*

7.2 (a) Raman spectrum of pristine-MoS_2 and MoS_2-WS_2 heterostructures (b) PL spectra of pristine-MoS_2 and MoS_2-WS_2 heterostructures. XPS spectra of pristine-MoS_2 and MoS_2-WS_2 heterostructures (c) Mo 3d, (d) S 2p, and (e) W 4f peaks, respectively *118*

7.3 Self-powered Electrical characterizations and photoresponse characteristics MoS_2-WS_2 heterostructure devices. (a) Schematic of the device. Current-voltage (I-V) characteristics measured in the dark and under different wavelengths. (b) Dark current, (c) Pristine-MoS_2, (d) MoS_2-WS_2 heterostructure, (e) I–V curves of the pristine-MoS_2 and MoS_2-WS_2 heterojunction under light illumination (580 nm, 120 μW/cm2), and (f) Comparison of semi-logirthm I-V of Pristine MoS_2 and MoS_2-WS_2 in the dark condition and light illumination (580 nm, 120 $\mu W/cm^2$ *120*

7.4 Photoresponse characteristics of self-powered device. (a) Responsivity, (b) Detectivity, (c) EQE of pristine MoS_2 and MoS_2-WS_2 under irradiation of Visible-NIR spectrum, respectively with an input power density (Pin) of 120 μW/cm2, (d, e) Responsivity and Detectivity with function of different incident optical power density, and (f) Comparison of Responsivity of pristine MoS_2 and MoS_2-WS_2 under light illumination of 580nm with various bias voltages. *121*

7.5 Comparative transient of pristine MoS_2 and MoS_2-WS_2 heterostructure with (a, b) Wavelength-dependent photoresponse, (c, d) different incident optical power density, and (e, f) Transient photoresponse measurement at different bias voltage at 580 nm wavelength of light at an incident optical power of 120 $\mu W/cm^2$ *122*

7.6 Rise time and fall time of (a) Pristine MoS2, (B) MoS2-WS2 heterojunction, and (c, d) Long-term stability of Pristine MoS2 and MoS2-WS2 heterostructure device with 100 cycles under 580 nm light illumination after 30days in ambient air *123*

7.7 Hysteresis behavior of I–V as a function of different sweeping rates (a) 1V/s, (b) 500 mV/s, (c) 100 mV/s, (d) 10 mV/s, with inset graph showing the magnified I-V of device, and (e) Schematic of the defects generate charge redistribution in pristine MoS2 *126*

7.8 Raman mapping of Pristine MoS2 (a, b) position mapping shows clear intensity difference between E2g and A1g mode, (c, d) and KPFM study of Pristine MoS2 (e-f) mapping of variation in thickness, (g, h) Surface potential images for pristine-MoS2 *126*

7.9 (a) Schematic illustration of the measurement configuration for the modulation of light, and (b-d) Representative photoresponse of the heterojunction photodiode under 580 nm light illumination with the modulated chopper frequency of 1 Hz, 100 Hz, and 1kHz respectively, Band alignment and charge transfer at the heterostructures. (e) a sketch of WS2 particle-decorated on MoS2-based photodetector, and (f) Schematic of Band profiles of MoS2 and WS2, which forms a type II heterojunction relative to the vacuum level. *128*

List of Tables

Table	*Title*	*page*
1.1	Comparison among different structures of MoS_2	*4*
4.1	Comparison of Various MoS_2 materials based NO_2 gas sensor	*80*
5.1	Comparison of the NO_2 sensors based on SnS_2 materials	*92*
5.2	A comparison of NO_2 sensor sensing performance based on 2D material	*98*
6.1	Adsorption energies of NO_2 gas over different surface systems. The structural changes in configurations are given by bond lengths and bond angles of the constituent elements	*105*
6.2	Adsorption energy and equilibrium distance along with charge transfer of the developed adsorption systems	*107*
6.3	Calculated gas adsorption energies of the gas adsorbed over SnS_2 surface	*109*
6.4	A summary of forward rate ($k_{ir(ads)}$) constant and maximum response of pristine SnS_2 and nitrogen plasma SnS_2 for various concentration of NO_2 at various operating temperatures using irreversible adsorption	*113*
6.5	Values of various parameter derived by fitting of the response curve as a function of concentration.	*113*
7.1	Comparison of self-powered photodetector figure of merit	*124*

List of Symbols

Symbol	*Description*
θ	Angle of incident
A	Area
E_g	Bandgap energy
Φ_B	Barrier height
k	Boltzmann constant
V_{bi}	Build-in potential
ΔI	Change in current
ΔR	Change in resistance
ΔV	Change in voltage
ΔEc	Conduction band offset
I_a or I_o	Current in air
I_g	Current in the target gas
E_c	Conduction band energy
τ_d	Decay time
I_d	Dark Current
D*	Detectivity of photodetector
W	Depletion width
q	Electron charge
G	Electron conduction
χ	Electron effinity
μ	Electron mobility
$q\ \phi_r$	Energy difference in conduction band and Fermi level
υ	Frequency
η	Ideality factor
Pi	Input power
c	Lattice constant
l	Length
Φ_m	Metal work function
T	Operating temperature
h	Plank constant
I_p	Photocurrent
n	Power coefficient
S	Relative response
R_a	Resistance in air
R_g	Resistance in the target gas
R	Responsivity of photodetector
A^*	Richardson constant
τ_r	Rise time
E_v	Valance band energy
ΔE_v	Valance band offset
V_a	Voltage in air
V_g	Voltage in the target gas
λ	Wavelength
W	Watt

List of Abbreviations

Abbreviation	Full form
2D	Two-dimensional
TMDs	T Transition metal dichalcogenides
AFM	Atomic force microscopy
BE	Binding energy
CL	Cathodoluminescence
CVD	Chemical vapor deposition
I-V	Current-voltage
D	Dimentional
DFT	Density functional theory
FESEM	Field emission scanning electron microscopy
FWHM	Full-width half maxima
FET	Field-effect transistor
HA	Horizontally aligned
IoT	Internet of Things
LED	Light-emitting diode
LDL	Low detection limit
MFC	Mass flow controller
MOCVD	Metal-organic chemical vapour deposition
Mo	Molybdenum
MoS_2	Molybdenum disulfide
Sn	Tin
SnS_2	Tin disulfide
1D	One-dimensional
PL	Photoluminescence
PVD	Physical vapour deposition
ppm	Parts per million
ppb	Parts per billion
RF	Radiofrequency
WS_2	Tungsten disulfide
RMS	Root mean square
RT	Room temperature
RH	Relative humidity
NPs	Nanoparticles
SEM	Scanning electron microscopy
S	Sulfur
Sv	Sulfur vacancy
SCCM	Standard cubic centimetres per minute
TE	Thermionic emission
Pt	Platinum
Pd	Palladium
Au	Gold
Ag	Silver
Uv-Vis	Ultraviolet- visible
VOC	Volatile organic compound
VA	Vertically aligned
XPS	X-ray photoelectron spectroscopy
XRD	X-ray diffraction

0D	Zero-dimensional
N	Nitrogen
JCPDS	Joint Committee of Power Diffraction Standards
EDX	Energy dispersive X-ray spectroscopy
KPFM	Kelvin probe force microscopy
Ar	Ar
O_2	Oxygen
CO_2	Carbon dioxide
NO_2	Nitrogen dioxide
NH_3	Ammonia
H_2	Hydrogen
CO	Carbon monoxide
H_2S	Hydrogen sulfide
SO_2	Sulfur dioxide
Vis	Visible
NIR	Near-infrared
nm	Nanometer
I_{photo}	Photocurrent
I_{dark}	Dark current
PDCR	Photo-to-dark current ratio
P	Incident power
A	Active area
R	Responsivity
D*	Specific detectivity
EQE	External quantum efficiency
SNR	Signal to noise ratio
NEP	Noise equivalent power
h	Planck constant
T_{rise}	Rise time
T_{fall}	Fall time
α	Absorption coefficient